Optics Letters

Proof of concept demonstration of a metastable helium fluorescence lidar for thermospheric wind and temperature measurements

Bernd Kaifler[1,*] and Christopher Geach[2]

[1]Deutsches Zentrum für Luft- und Raumfahrt, Institut für Physik der Atmosphäre, Oberpfaffenhofen 82234, Germany
[2]Deutsches Zentrum für Luft- und Raumfahrt, Institut für Solar-Terrestrische Physik, Neustrelitz 17235, Germany
*bernd.kaifler@dlr.de

Received 2 May 2024; revised 20 June 2024; accepted 10 July 2024; posted 11 July 2024; published 31 July 2024

We report on the first, to the best of our knowledge, spectral measurements of terrestrial thermospheric metastable helium using ground-based lidar. By stimulating fluorescence of He(2^3S) at four closely spaced wavelengths within the He line around 1083 nm and measuring the lidar returns, we measured the He(2^3S) spectrum at 600 km, providing coarse constraints on the He(2^3S) temperature and vertical wind speed. This work serves as a proof of concept and precursor experiment for future, more powerful helium lidar systems capable of measuring vertical profiles of neutral wind and temperature in the upper terrestrial thermosphere.

https://doi.org/10.1364/OL.528925

Fluorescence lidars probing the absorption lines of metallic atoms have been used to measure temperature and wind in the mesosphere/lower thermosphere region (approximately 80–100 km altitude) in the Earth's atmosphere for the last four decades [1–6]. While these lidar instruments have been steadily improved to achieve better time resolution and higher accuracy, efforts to extend the fluorescence lidar technique into the upper thermosphere (250–1000 km) have been largely unsuccessful because the number density of metallic species decreases rapidly with altitude above 100 km. The greatest achieved heights so far reported are the successful detection of lidar returns of calcium ions (Ca^+) at 300 km [7], neutral sodium (Na) at 200 km [8], and neutral iron (Fe) at 155 km [9]. Given the low number densities of few atoms cm^{-3} at these altitudes, the lidar returns were extremely weak, and no temperatures or wind speeds could be derived from the measurements, with the exception of [9] who report temperatures up to 150 km but with estimated errors exceeding 30%. Similarly, [10] derived temperatures up to 140 km and winds up to 115 km based on Na measurements. So far there are no remote sensing techniques that provide vertically resolved measurements of neutral wind in the upper thermosphere, and *in situ* measurements by sounding rockets tend to be sparse in geographic location and time.

Probing metastable helium He(2^3S) instead of metallic species offers the prospect of achieving measurements at heights well above 500 km because of the large abundance of helium in the outer layers of the Earth's atmosphere in comparison to metallic species. While ground-state helium He(1^1S) cannot be excited by ground-based lidar due to the large required energy (19.8 eV, corresponding to a photon wavelength of 62.6 nm), the metastable He(2^3S) can be further excited to the 2^3P state through absorption of a photon with 1083 nm wavelength, giving rise to fluorescence. (Similarly, He(2^3S) can be excited to the 3^3P state through absorption of a photon with 389 nm wavelength, but the strength of this transition is >10× weaker than the transition to the 2^3P state.) Since the transition from the 2^3S state to the ground state through single-photon processes is forbidden, the 2^3S state has a long natural lifetime of ~7800 s. This long lifetime can lead to the buildup of a significant population of He(2^3S), either through excitation of He(1^1S) by the impact of energetic photoelectrons or through recombination of He^+ [11], producing a measurable airglow signal when sufficiently illuminated [12]. Penning ionization effectively quenches He(2^3S) below 250 km altitude, and photoionization is the primary sink at higher altitudes. The result is a layer of He(2^3S) which extends from about 250 km altitude to above 800 km with peak densities of few atoms cm^{-3} [11,13].

The 2^3P state of ^{4}He splits into three sublevels. Two transitions of the triplet which connects the 2^3P state to the 2^3S state blend together at temperatures larger than ~450 K, while the third transition is offset by −125 pm relative to the strongest transition (see Table 1). In the terrestrial He(2^3S) layer, the line shape is fully dominated by thermal Doppler broadening.

Following [15], the backscattered signal $S(\lambda, \rho, T, w)$ obtained by a vertically oriented lidar measuring at wavelength λ, given a He(2^3S) layer with number density ρ, temperature T, and vertical wind w, may be written as

$$S(\lambda, \rho, T, w) = \eta \left(\frac{P_L \tau}{E_\gamma}\right) (\rho \sigma \Delta z) \left(\frac{A}{4\pi z^2}\right) + N_B, \qquad (1)$$

where η is the end-to-end coupling efficiency of the lidar system (encompassing atmospheric transmission, beam and field-of-view overlap, receiver transmission, detector efficiency, etc.), P_L is the output power of the laser, τ is the integration time,

Table 1. Spectroscopic Properties of He Transitions Around 1083 nm[a]

No.	Transition	Vac. Wavelength (nm)	Offset Wavelength (pm)	Offset Frequency (GHz)	Oscillator Strength
1	2^3S_1–2^3P_2	1083.3306444	0	0	0.29948
2	2^3S_1–2^3P_1	1083.3216751	−8.97	2.2911	0.17969
3	2^3S_1–2^3P_0	1083.2057472	−124.90	31.9045	0.05990

[a]Values are from [14].

E_γ is the energy per photon, z is the altitude, Δz is the altitude range, A is the receiving area of the telescope, and N_B is the altitude-independent background noise. $\sigma(\lambda, T, w)$ is the scattering cross-section of the metastable helium and can be written as

$$\sigma(\lambda, T, w) = \sum_{n=1}^{3} \sigma_n(\lambda, T, w)$$
$$\sigma_n(\lambda, T, w) = C\sqrt{\frac{D_n}{\pi T}} f_n \exp\left[-\frac{D_n}{T}(\lambda - \lambda_n - \lambda w/c)^2\right], \quad (2)$$

where σ_n are the contributions to the scattering cross-section from the individual components of the multiplet, λ_n are the wavelengths of the individual components, and f_n are the dimensionless oscillator strengths. $D_n = c^2 m/(2k_B\lambda_n^2)$ with the speed of light c, the mass of a ^{4}He atom m, and the Boltzmann constant k_b; and $C = e^2/4\epsilon_0 m_e c$, with the electrical charge of an electron e, the mass of an electron m_e, and the permittivity of free space ϵ_0. The values of the spectroscopic parameters are given in Table 1.

For lidar observations, it is beneficial to target the strongest transition because it provides the largest lidar returns and thus the greatest signal-to-noise ratio. Figure 1 shows the variation of the scattering cross-section of the first two transitions with wavelength for several temperatures. We note that the wavelength corresponding to the maximum cross-section shifts slightly with temperature and that the spectrum is not symmetric, due to the superposition of two lines with unequal strength.

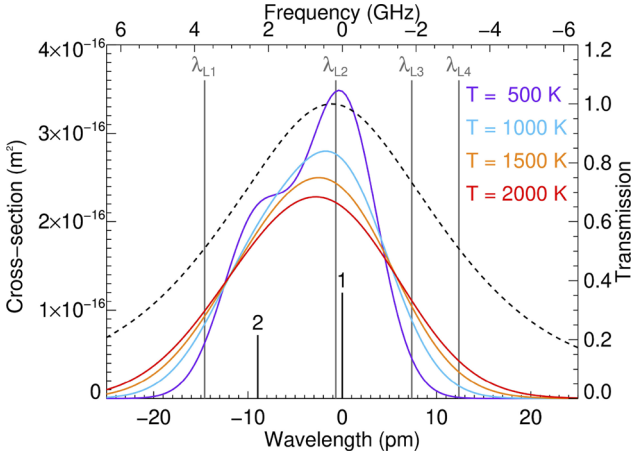

Fig. 1. Simulated Doppler-broadened spectrum of He(2^3S) for a range of temperatures, plotted relative to a reference wavelength of 1083.33065 nm (vac). The black vertical lines mark the two transitions $2^3P_2 \rightarrow 2^3S_1$ (1) and $2^3P_1 \rightarrow 2^3S_1$ (2), and the gray lines mark our selected measurement wavelengths. The dashed line depicts the transmission of the narrowband optical filter in the receiver, normalized to unity.

The helium fluorescence lidar was first proposed in the late 1990s [15]. However, technical challenges including the development of a pulsed laser source and an efficient low-noise single-photon detector operating at 1083 nm wavelength prevented the successful realization for more than two decades. Only recently was the detection of He(2^3S) by lidar finally demonstrated [13]. Now we have improved the setup described in [13] to allow for spectral measurements. The pulse energy of the injection-seeded Q-switched Nd:$GdVO_4$ laser was increased to 4.7 mJ by adding a double-pass amplifier, resulting in a mean output power of 0.54 W at a 115 Hz pulse repetition frequency. Lowering the pulse frequency was necessary to avoid pulse overlap resulting from the metastable He layer extending beyond 800 km altitude. We also added the capability to tune the laser wavelength by thermally tuning the distributed feedback laser diode that is used as the seed laser. The wavelength of the pulsed laser is measured with a wavemeter (TOPTICA WS6-200), and a software control loop sends the control signal to the seed laser. The RMS fluctuations of the laser wavelength are 0.1 pm, and the absolute accuracy of the wavemeter is 0.8 pm. The wavelength of each laser pulse is measured, and the information is stored together with the lidar returns in the raw data files. No changes were made to the lidar receiver with respect to [13], except for the addition of a mechanical chopper that blocks the optical signal from the lower 15 km of the atmosphere to avoid saturation of the detector. Backscattered photons collected with a fiber-coupled telescope with a 762 mm diameter and a 61 μrad field of view (FOV) are spectrally filtered by a filter stage comprising a 0.7 nm wide multi-cavity coarse filter and two air-gapped narrowband etalons, with a combined effective bandwidth of 29.7 pm. The detection system is a custom-made superconducting nanowire single-photon detector (SNSPD) with ~30% detection efficiency at a 1083 nm wavelength and ~70 Hz dark counts. Recorded raw data are timestamps corresponding to the arrival times of detected photons relative to the firing time of the pulsed laser. The resolution of the employed time tagger is 0.8 ns. The overlap between the laser beam and the telescope FOV is maintained using the conical scan technique [16]. More information on the instrument setup can be found in [13].

In a first proof of concept demonstration, we sampled the Doppler-broadened absorption line of He(2^3S) at four wavelengths: λ_{L1} = 1083.316 nm, λ_{L2} = 1083.330 nm, λ_{L3} = 1083.338 nm, and λ_{L4} = 1083.343 nm. The wavelengths represent a point at approximately 30% of the maximum on the blueshifted side, the maximum, a point at approximately 30% of the maximum on the redshifted side, and the redshifted tail, respectively (see Fig. 1). They were chosen as a compromise between maximizing the return signal, i.e., probing the line where the scattering cross-section is largest, and the ability to determine the linewidth. Maximizing the return signal is of particular importance given the weak signal: with our current setup, we expect about one detected fluorescence photon for every 200 laser pulses, which is about one photon every 2 s. While measurements at three wavelengths are generally sufficient to determine the linewidth (temperature), the amplitude (He(2^3S) number density), and the Doppler shift due to the line-of-sight wind, we added a fourth

wavelength for consistency checks. Selecting a wavelength located in the tail of the distribution also gave us the opportunity to study the performance of the lidar at extremely low signal levels. The laser wavelengths were switched under software control in the sequence $\lambda_{L1}, \lambda_{L2}, \lambda_{L3}, \lambda_{L4}, \lambda_{L4}, \lambda_{L3}, \lambda_{L2}, \ldots$ with a dwell time of 30 s at each wavelength. Laser pulses with wavelengths outside a window of ±0.5 pm of the nominal wavelengths occurred sporadically during tuning from one wavelength to another. These laser pulses accounted for 20% of the total and were excluded in the data analysis.

For this study, we selected six lidar observations that were acquired at the site of the German Aerospace Center in Oberpfaffen-hofen, Germany (48°N, 11°E) between 20 and 29 January 2024. Since the expected He(2^3S) density is largest just before sunrise [13], we limited the dataset to periods with solar elevation angles between −40° and −7° to maximize the signal-to-noise ratio. After performing quality checks on the data, such as removing periods with elevated background due to the presence of clouds (see [13] for details), 13.9 h with observations remain. Binned photon counts are shown in Fig. 2. Below an altitude of about 15 km, the optical signal path is blocked by a mechanical chopper in the receiver in order to protect the detector from excessive high count rates. Above, up to an altitude of about 100 km, the photon counts are dominated by the strong Rayleigh scattering. Above 100 km, most of the signal comes from detector dark counts, He(2^3S) fluorescence stimulated by sunlight, and other sources of light (e.g., scattered moonlight). All these sources have in common that they are approximately constant in time within the round trip time of a laser pulse to 1300 km altitude (~8.7 ms), and their contributions to the lidar signal can be estimated as an altitude-independent background. We use the altitude range 100–250 km to estimate this background, as this region is above the maximum altitude where any significant Rayleigh scattering can be expected and below the minimum altitude where we can expect helium fluorescence [11]. Increasing the binning to 100 km and zooming in on the background line reveals the fluorescence induced by the laser light (right panel in Fig. 2). However, the fluorescence signal is very weak: at its peak from 500 to 600 km, the fluorescence at the central wavelength λ_{L2} amounts to just ~3200 counts, about 3.5% of the background. At the shifted wavelengths, the counts are substantially lower, due to the lower scattering cross-section and lower filter transmission (see Fig. 1).

We extracted spectral information from the data first by subtracting a range-independent background and then by calibrating the excess return counts based on the Rayleigh returns from altitudes between 36 and 50 km; this procedure is described in detail in [13].

In addition to these steps, an additional spectral correction is required, due to the differing transmission of the receiver optical filter for Rayleigh and fluorescence returns, due in turn to the differing wavelengths of these two signals. Rayleigh scattering results in return wavelengths that are Doppler-broadened about the emitted wavelength, within practical limits (we neglect the Doppler shift due to the vertical wind, which is approximately zero within normalization height range), whereas fluorescent scattering results in return wavelengths that are mirrored about the respective absorption lines (see, e.g., [17]). That is, for a photon emitted from the laser with a wavelength λ_E and a fluorescence line with a wavelength λ_F, the return photon will have a wavelength $\lambda_R = \lambda_F + (\lambda_F - \lambda_E) = 2\lambda_F - \lambda_E$. This is due to the fact that fluorescence only occurs for those atoms in whose rest frame the wavelength of the emitted photon precisely matches the absorption line. The relative motion of the atom and laser produces a Doppler shift twice, once upon absorption and again upon emission, resulting in a return photon with a wavelength that is mirrored about the absorption line. The receiver transmission is therefore in general different for the Rayleigh and fluorescent return signals.

The first step to correct for this effect was to measure the relative transmission spectrum of the optical filter in the receiver. This was performed by coupling a tunable ECDL laser into the receiver and measuring the output with a photodiode. The resulting spectrum was then fit with a linear combination of a Gauss and an Airy function with equal weighting. The result is shown as the dashed curve in Fig. 1; we refer to the resulting transmission function as $\beta(\lambda)$. Due to a slow leak in one of the two etalon pressure vessels, the overall transmission spectrum drifted by ~0.5 pm per day. Multiple measurements confirmed that the shape of the spectrum remained stable despite the leak. We again used the Rayleigh signal between 36 and 50 km to fit for this drift, and we adjusted the measured transmission spectrum for each measurement independently. We then defined a correction factor $\alpha(\lambda_{Li})$ for fluorescence returns at wavelength λ_{Li}, with

$$\alpha(\lambda) = \frac{\beta(\lambda)}{\beta_R(\lambda)}; \quad \beta_R(\lambda) = \frac{\sum_{n=1}^{3} \sigma_n(\lambda, T, w)\beta(2\lambda_n - \lambda)}{\sigma(\lambda, T, w)}, \tag{3}$$

where $\beta_R(\lambda)$ gives the average receiver transmission of the helium return signal for a given laser wavelength. The effect of Doppler broadening of the Rayleigh return signal on receiver transmission is on the order of 1%, and we ignore it. We similarly ignore the wavelength dependence of the Rayleigh scattering cross-section; over our observation range, this would amount to a <0.01% correction. Finally, $\alpha(\lambda_{Li})$ depends on the temperature and vertical winds of the He(2^3S) layer, but this dependence is rather weak. We assumed a temperature of 1000 K and no vertical winds, and we note that $\alpha(\lambda_{Li})$ changes by approximately 0.5% per 100 K.

Figure 3 shows the background-subtracted, calibrated, and corrected measurements $\alpha S_F/S_R$, where S_F and S_R are the background-subtracted fluorescence and Rayleigh returns, respectively. S_F has been integrated over an altitude range from

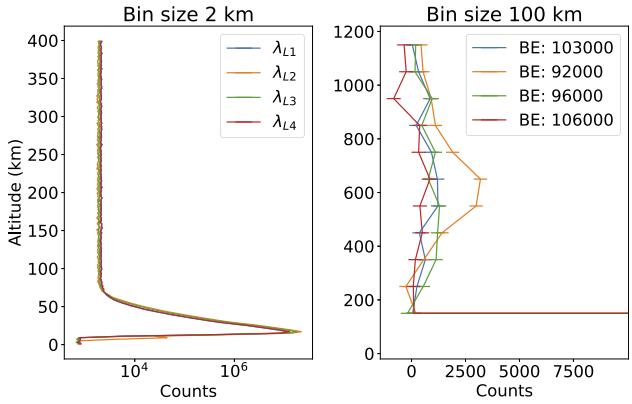

Fig. 2. Binned photon counts obtained at each measurement wavelength. The helium fluorescence signal (right panel, above 300 km) is small compared to the Rayleigh returns from the lower atmosphere (left panel, below 100 km). Background estimates (BEs) have been subtracted from the profiles in the right panel; the magnitudes are given in the legend.

500 to 700 km, and the plot has been scaled vertically to the measured value at λ_{L2} (the fitting procedure described below, however, was applied to the unscaled measurements). The error bars mark the 1σ-uncertainties of the measurements determined from photon count statistics (shot noise) and error propagation. Although the errors are quite large, it is possible to fit ρ, T, and w in Eq. (1) using a least squares optimization algorithm to obtain realistic estimates for these parameters. Due to the nonlinear nature of the fitting function with respect to the fit parameters, we estimated the errors on the fit parameters using a Monte Carlo simulation: we generated $N = 1000$ sets of synthetic data, drawn from Gaussian distributions determined by the original measurement values and uncertainties at the respective wavelengths. For each set of synthetic data, we again used Eq. (1) to obtain a set of synthetic fit parameters. For each fit parameter, we found the 16th and 84th percentile values of the corresponding set of synthetic fit parameters and defined this range to be the 1σ confidence interval (CI).

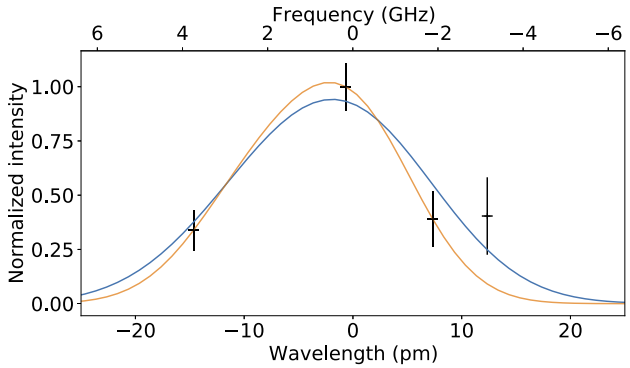

Fig. 3. Measured He(2^3S) fluorescence spectrum (black points) and fitted theoretical spectra based on all four data points (blue curve) or omitting λ_{L4} (orange curve), plotted relative to 1083.33065 nm (vac) and scaled by the measured value at λ_{L2}. The altitude range is 500–700 km.

Using all four available data points, we obtain $\rho = 1.64$ cm^{-3} (CI: 1.46–1.89 cm^{-3}), $T = 2230$ K (CI: 1360–3580 K), and $w = 270$ m/s (CI: −60–730 m/s) (blue line in Fig. 3). When omitting the fourth data point (λ_{L4}) that has the largest error, the estimates change to $\rho = 1.48$ cm^{-3} (CI: 1.32–1.67 cm^{-3}], $T = 1260$ K (CI: 830–1790 K), and $w = 20$ m/s [CI: −220–330 m/s] (orange line in Fig. 3). Note that the number density is consistent with previous predictions [11] and that these temperature estimates, though higher than what is generally assumed at these altitudes, are consistent with the temperatures in [18], who passively measured the spectrum of the He(2^3S) airglow signal, thereby inferring temperature. As argued in that paper, these higher temperatures could indicate that recombination of hot He^+ plays a larger than expected role in the formation of the He(2^3S) layer. However, given the large uncertainties associated with the present measurements, this conclusion is far from clear.

Note that the above discussion includes only uncertainty arising from photon noise; any treatment of the line shape of the laser, fluctuations in the laser wavelength, or a potential offset in our wavelength calibration has been omitted. For future measurements, a Doppler-free spectroscopy system (currently in development) will be used to characterize the laser and account for related spectral effects, as in [19].

In conclusion, we have demonstrated spectral measurements of He(2^3S) by ground-based lidar. We note that the uncertainty of retrieved parameters based on our measurements is large; however, there are straightforward ways to improve the throughput of our experiment setup, e.g., using a more efficient and larger detector coupled to a large aperture telescope. A SNSPD with 70% quantum efficiency at 1550 nm wavelength coupled to the 5.1 m Hale telescope at Palomar Observatory was recently demonstrated for deep space optical communication [20]. Using this setup as a lidar receiver would improve the signal by more than two orders of magnitude. Also, a tenfold increase in laser power based on existing technology seems achievable. Based on these prospects, the metastable helium fluorescence lidar has the potential to become a new tool for ground-based measurements of temperature and neutral wind in the upper thermosphere.

Funding. Deutsches Zentrum für Luft- und Raumfahrt.

Acknowledgment. We acknowledge the work of Christian Büdenbender in upgrading the laser and thank Andreas Mezger for the help with setting up and operating the experiment.

Disclosures. The authors declare no conflicts of interest.

Data availability. Data underlying the results presented in this paper may be obtained from the authors upon reasonable request.

REFERENCES

1. M. R. Bowman, A. J. Gibson, and M. C. W. Sandford, Nature **221**, 456 (1969).
2. K. Fricke and U. von Zahn, J. Atmos. Terr. Phys. **47**, 499 (1985).
3. C. Y. She and J. R. Yu, Geophys. Res. Lett. **21**, 1771 (1994).
4. C. Y. She, J. D. Vance, B. P. Williams, *et al.*, Eos Transactions **83**, 289 (2002).
5. T. D. Kawahara, S. Nozawa, N. Saito, *et al.*, Opt. Express **25**, A491 (2017).
6. T. Li, C. Ban, X. Fang, *et al.*, Atmos. Chem. Phys. **18**, 11683 (2018).
7. J. Jiao, X. Chu, H. Jin, *et al.*, Geophys. Res. Lett. **49**, e2022GL100537 (2022).
8. Y. Xun, G. Yang, C.-Y. She, *et al.*, Geophys. Res. Lett. **46**, 1892 (2019).
9. X. Chu, Z. Yu, C. S. Gardner, *et al.*, Geophys. Res. Lett. **38**, L23807 (2011).
10. A. Z. Liu, Y. Guo, F. Vargas, *et al.*, Geophys. Res. Lett. **43**, 2374 (2016).
11. L. S. Waldrop, R. B. Kerr, S. A. González, *et al.*, J. Geophys. Res.: Space Phys. **110**, A08304 (2005).
12. A. V. Mironov, V. S. Prokudina, and N. N. Shefov, in *Spectral, Electrophotometrical, and Radar Studies of Aurorae and Airglow* (1959), pp. 20–24.
13. B. Kaifler, C. Geach, H. C. Büdenbender, *et al.*, Nat. Commun. **13**, 6042 (2022).
14. G. W. F. Drake and D. C. Morton, Astrophys J. Suppl. S. **170**, 251 (2007).
15. A. J. Gerrard, T. J. Kane, D. D. Meisel, *et al.*, J. Atmos. Sol.-Terr. Phys. **59**, 2023 (1997).
16. B. Kaifler and N. Kaifler, Atmos. Meas. Tech. **14**, 1715 (2021).
17. C.-Y. She, H. Chen, and D. A. Krueger, J. Opt. Soc. Am. B **32**, 1575 (2015).
18. R. B. Kerr, J. Noto, R. S. Lancaster, *et al.*, Geophys. Res. Lett. **23**, 3239 (1996).
19. D. A. Krueger, C.-Y. She, and T. Yuan, Appl. Opt. **54**, 9469 (2015).
20. E. Wollman, J. Allmaras, A. Beyer, *et al.*, in *Free-Space Laser Communications XXXVI*, H. Hemmati and B. S. Robinson, eds., International Society for Optics and Photonics (SPIE, 2024), Vol. 12877, paper 128771H.